UKAEA-CCFE-PR(23)159

J W Berkery, S A Sabbagh, C Ham, V Zamkovska, J Butt, J Riquezes, M Tobin, S Henderson, L Kogan, B Patel, R Scannell, E Trier, B LeBlanc

Density Limits as Disruption Forecasters for Spherical Tokamaks

Density Limits as Disruption Forecasters for Spherical Tokamaks

J W Berkery, S A Sabbagh, C Ham, V Zamkovska, J Butt, J Riquezes, M Tobin, S Henderson, L Kogan, B Patel, R Scannell, E Trier, B LeBlanc

IOP Publishing Plasma Physics and Controlled Fusion
Plasma Phys. Control. Fusion **XX** (XXXX) XXXXXX https://doi.org/XXXX/XXXX

Density Limits as Disruption Forecasters for Spherical Tokamaks

J W Berkery[1], S A Sabbagh[2], C Ham[3], V Zamkovska[2], J Butt[2], J Riquezes[2], M Tobin[2], S Henderson[3], L Kogan[3], B Patel[3], R Scannell[3], E Trier[3], B LeBlanc[1]

[1] Princeton Plasma Physics Laboratory, Princeton, NJ 08543, United States of America
[2] Department of Applied Physics and Applied Mathematics, Columbia University, New York, New York 10027, USA
[3] Culham Centre for Fusion Energy, UKAEA, Abingdon, OX14 3DB, UK

E-mail: jberkery@pppl.gov

Received xxxxxx
Accepted for publication xxxxxx
Published xxxxxx

Abstract

Fusion power output from spherical tokamaks would benefit from increased confined plasma density, but there exists a limit on the density before confinement is lost and the plasma current is disrupted. This density limit has long been characterized by a simple, global Greenwald limit proportional to the plasma current and inversely proportional to the cross sectional area of the plasma. It is shown that in the database of discharges from the NSTX and MAST spherical tokamaks, the likelihood of disruption does increase above the Greenwald limit, and especially in the plasma current rampdown phase. The physics of the density limit has been recently theoretically explored through local criteria. Several of these are tested using the disruption event characterization and forecasting (DECAF) code for their potential effectiveness as disruption warning signals. For a limited set of NSTX discharges, a local island power balance criteria was found to be less reliable, presently, than the Greenwald limit. An empirical critical edge line density and a boundary turbulent transport limit were both tested for MAST-U, which has a detailed electron density profile measurement. Both were found to have similar dependencies. In a limited set of MAST-U discharges that appear to disrupt due to rising density at values under the Greenwald limit, crossing of the boundary turbulent transport limit occurred close to the time of disruption. Finally, these limits were evaluated for their potential use in real-time, and it was found that with the necessary real-time inputs and with refinement through further testing, these limits could be implemented in a real-time disruption forecasting system.

Keywords: density limit, disruptions, tokamak

(Some figures may appear in colour only in the online journal)

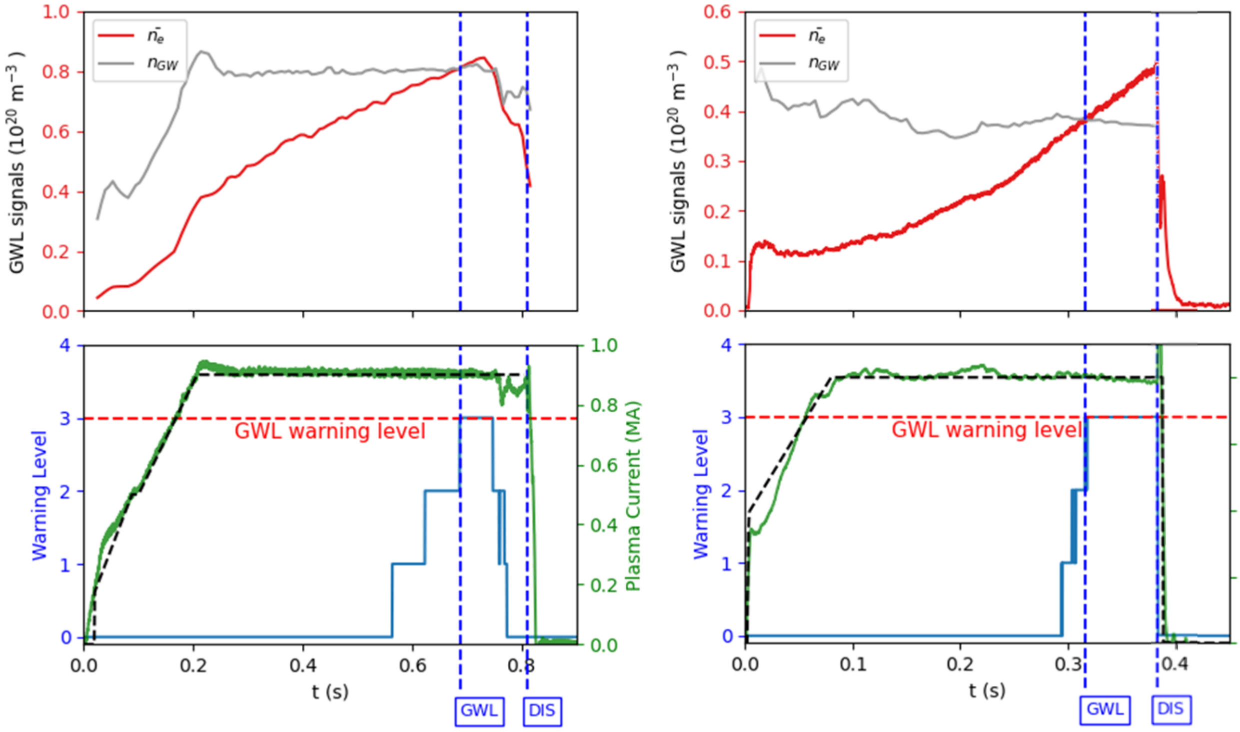

Figure 1: Example NSTX (134031) and MAST (27826) discharges that disrupt after crossing the Greenwald limit in the flattop. The top plots show the measured line averaged density and calculated Greenwald density. The bottom plots show the plasma current and requested plasma current (dashed), as well as the DECAF warning level (0 to 3) for the Greenwald limit (GWL event declared at level 3) and DECAF determination of the disruption time (DIS).

1. Introduction

Tokamaks confine fusion plasmas in magnetic fields that are partially created by current flowing in the plasmas themselves. Unfortunately, the plasma current is prone to disruption by instabilities in the plasma confinement. When the plasma current disrupts, it can quickly go to zero, destroying the confining field and releasing the stored energy of the plasma to the surrounding structures, potentially damaging them. The long-known density limit is an indicator of disruptions in tokamaks. This limit has been expressed in a global sense through the Greenwald limit [1,2]: line average density n_e [10^{20}m^{-3}] < $n_G \equiv I_p$ [MA] / πa^2 [m^2], where I_p is the plasma current and a is the plasma minor radius. Crossing of the density limit is just one event that can indicate susceptibility of a fusion plasma to disruption [3], but it is a critically important one. Fusion power output is proportional to the density squared, so a higher density is advantageous.

A related phenomenon is “radiative collapse” in tokamaks. When the power radiated away from the plasma by impurities reaches a large percentage of the input power, the energy balance of the plasma is upset and disruption can occur. This occurrence is sometimes associated with what is known as multifaceted asymmetric radiation from the edge (MARFE) [4]. These phenomena are all related because the impurity radiation may rise with density, and indeed may be the underlying cause of the density limit itself. Radiation, neutral particles, or plasma transport may cause the plasma edge or magnetic islands to cool, leading to redistribution of the current and growth of magnetohydrodynamic (MHD) modes of instability.

Recently it has been recognized that there is a need to monitor such disruptive events in real-time during tokamak operations. There are multiple high level strategies for a real-time plasma event monitor: detection of deviation of the plasma from expected state, and detection of known dangerous event chains. The first is important for future devices which may operate in a limited number of well-established plasma equilibria. The first strategy may use several methods as well, such as looking at deviation of measured quantities from pre-programmed values, real-time predictive simulations, machine learning (ML) algorithms, or values estimated by a plasma state observer. One example of this is the RAPTOR code alarm functions based on mismatch between measured and estimated radiated power and electron temperature [5]. This is being expanded to observer density estimation as well [6,7], with density measurements now being used to constrain a predictive transport model for the density evolution [8]. Feedback control of density in tokamaks has already begun to be implemented [9,10].

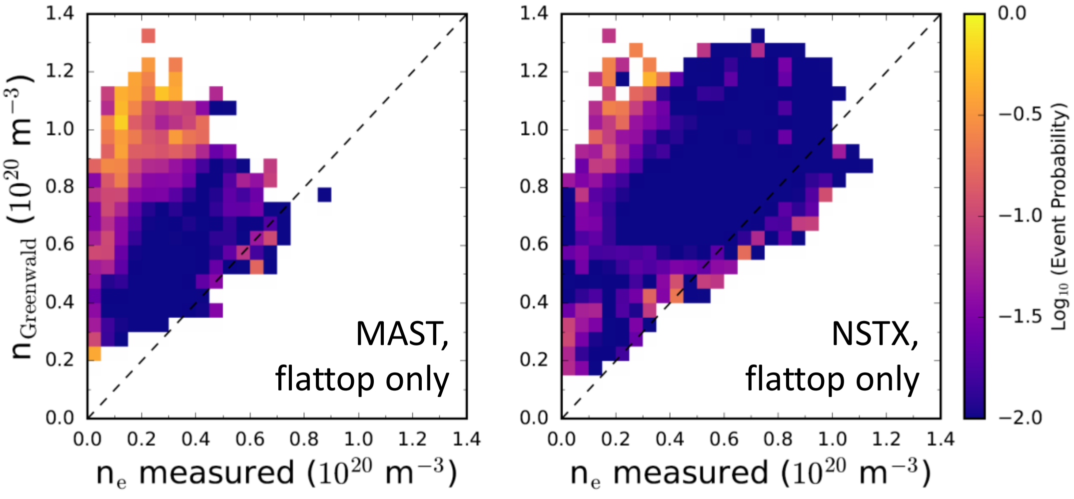

Figure 2: Disruptivity diagrams for the MAST and NSTX databases in the space of measured vs. Greenwald density, only for times in the flattop. Contours indicate the probability of disruption occurring in the database of plasmas in each section of parameter space.

ML techniques have begun to be applied to the density limit problem as well [11], for example using a radiation profile measurement as input for a neural network [12] or decision tree [13] in J-TEXT or using a long short-term memory network [14] or a random forest [15] in EAST. Additionally, Greenwald fraction (n_e/n_G) has been used as an input to random forest based [16] or deep learning [17] disruption prediction algorithms run on multiple machines, and it was found that it can be an important contributor [18].

The second strategy, which is more aligned with the capabilities of the Disruption Event Characterization and Forecasting (DECAF) code [19,20,21,22,23,24], is the detection of known dangerous event chains. DECAF is already carrying out statistical characterizations of current tokamak databases to identify common chains of events which lead to disruption. The common chains may, of course, vary by machine, for example: resistive wall mode event chains in the National Spherical Tokamak Experiment (NSTX [25]) were not common in the Mega Ampere Spherical Tokamak (MAST [26]) [19]. Once common chains are identified, real-time monitoring of plasma events can then be used to detect the chains. A plasma "health evaluator" can then cue the appropriate recovery or avoidance response, such as, for example, electron cyclotron heating aimed at the correct surface to stabilize MHD modes [27,28]. Sensors for early disruption detection related to density limits, such as MARFE detectors or critical density thresholds for MARFEs [29], measurements of density fluctuations associated with enhanced transport [30], or density or radiation peaking measurements, have been proposed [28]. In the ASDEX Upgrade (AUG) and TCV tokamaks a system monitoring the normalized edge density [31] and energy confinement time and comparing to empirical disruption limits has already been implemented in an off-normal event handler [32,33].

"Density limit" and "Greenwald limit" have long been practically synonymous in tokamaks. The Greenwald limit is simply formulated, which certainly has its advantages, but if the theory underlying the density limit can be better understood, it could lead to better forecasting of approaching disruptions. Recently theoretical investigation of the density limit has progressed, including a local density limit theory based on power balance in magnetic islands [34], a modification of the Greenwald limit based on including the effect of auxiliary heating [35], a ballooning stability limit at the separatrix [36], a power balance including radiation losses from impurities and neutrals [37], and a scaling law based on an increase in boundary turbulent transport with collisionality [38] to name a few.

The framework of the DECAF code, and its large database of discharge data from many machines represents an opportunity to test some of these theories. The present paper focuses on testing their utility for disruption forecasting in spherical tokamaks.

In the present paper we first present the DECAF database of NSTX and MAST disruptions, focussing on the Greenwald limit in the flattop in section 2. In section 3, the particular case of density limits in the plasma current rampdown is discussed. Section 4 focusses on edge density limits, in various forms, and considers their effectiveness by testing them against limited data sets from NSTX and MAST-U [39], the upgrade to MAST. Finally, in section 5 the usefulness of these edge limits as real-time disruption forecasters for spherical tokamaks is assessed and then the conclusions of the paper are drawn.

2. DECAF database of density and limit disruptions

2.1 Example density limits in NSTX and MAST

NSTX has been known to reach densities near the Greenwald limit from its early days [40,41]. As one of the first steps towards analysis of tokamak disruption data with DECAF, the straightforward GWL event was implemented. This means simply that the quantity n_G was calculated from measured I_p and equilibrium-reconstructed a, and was compared to measured line average density n_e. Multiple threshold levels of n_e/n_G can be set in DECAF with different warning levels to eventually feed into an event monitor, which can also eventually be operated in real-time in plasma operation. All analysis in the present paper was not performed in real-time, however.

Figure 1 shows example GWL events found in discharge 134031 from NSTX and 27826 from MAST. The time of disruption determined by DECAF is marked and labelled “DIS”. The line average density and Greenwald density are also shown, as well as the GWL warning levels 1, 2, and 3 from the Greenwald fraction reaching 0.90, 0.95, and 0.99, respectively. In these particular cases there is a 142 ms warning time between GWL (level 3) and DIS for NSTX, and 67 ms for the MAST discharge. These times are somewhat longer than usual, however, as will be shown.

2.2 Disruptivity diagrams

The DECAF code’s many separate physical event modules provide warnings and declare occurrences of certain events leading to disruption. The code also includes the ability to make diagrams showing either the operational space [42] or the probability of a DECAF event occurring within a given parameter space of tokamak operation [20]. Here, each colored square in parameter space is only plotted if at least 10 equilibrium (time) points from the database exist within that space. Most commonly the time of disruption, or DIS event, is used, resulting in a familiar disruptivity plot [43,44].

When plotted in the parameter space of measured vs. Greenwald density, these diagrams clearly illustrate the ubiquity of the Greenwald density limit between devices. This can be seen in Fig. 2 by the increased level of disruptivity along the diagonal line indicating the limit, and the limitation of the operational space of the devices to the space below the limit (to the left of the dashed line). These diagrams are a variation on so-called Hugill diagrams [45] (for example: [43,46,47,48,49,50,51]), which illustrate a similar point.

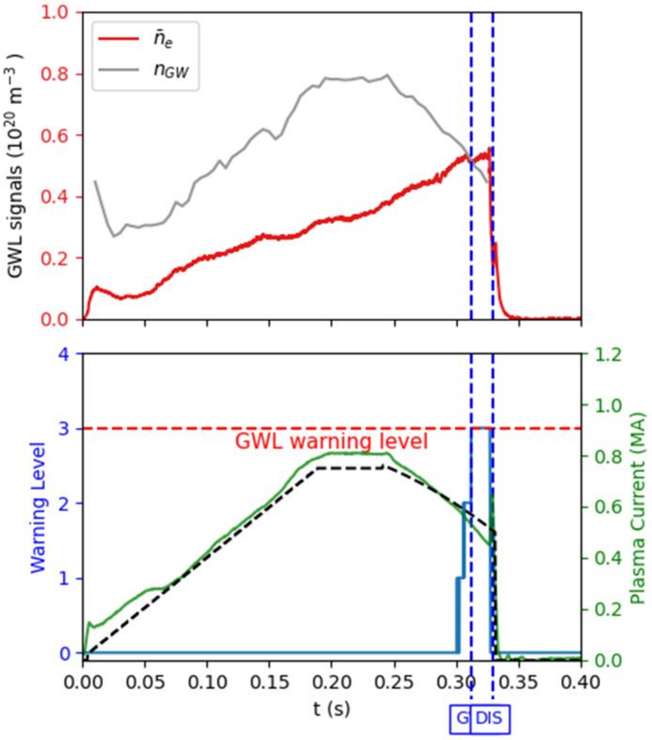

Figure 3: An example MAST discharge (26242) that disrupts after crossing the Greenwald limit in the rampdown.

The contours that are plotted in the diagrams show the number of times a discharge disrupted within a square of space divided by the total number of times that space was accessed. In Fig. 2, the squares have a width of Δn_e and height Δn_G of 5×10^{18}m^{-3}. For a specific example, in the square for MAST with n_e between 0.25-0.3$\times10^{20}$m^{-3} and n_G between 0.75-0.8$\times10^{20}$m^{-3}, there were 89 disruptions out of 2798 total equilibria, so the square is plotted with the color for Log$_{10}$(Event Probability) = -1.5. It should be noted that in the diagrams shown here, a square with zero disruptions is colored the same as the bottom contour, 10^{-2}. This means that anywhere from 0/10 occurrences to 1/100 to 100/10,000 (or more) are displayed identically. These diagrams, then, do not give a good sense of the total operational time a device spent in a given space. Another type of diagram plotting exactly that is of course possible as well [42], but not shown here. For example in Ref. [42] it was seen that in early operation of MAST-U a vast majority of the operation occurred well below the Greenwald limit.

Figure 2 uses the DECAF disruption databases for the NSTX and MAST devices. This includes 8,636 discharges in NSTX with 372,178 total flattop time points and 2,731 flattop disruptions. For MAST the corresponding numbers are 8,902, 215,208, and 4,396. Because of different nominal durations of discharges in each device the total number of time points analysed for each device varies as well. For example, in the diagrams shown here, the equilibrium

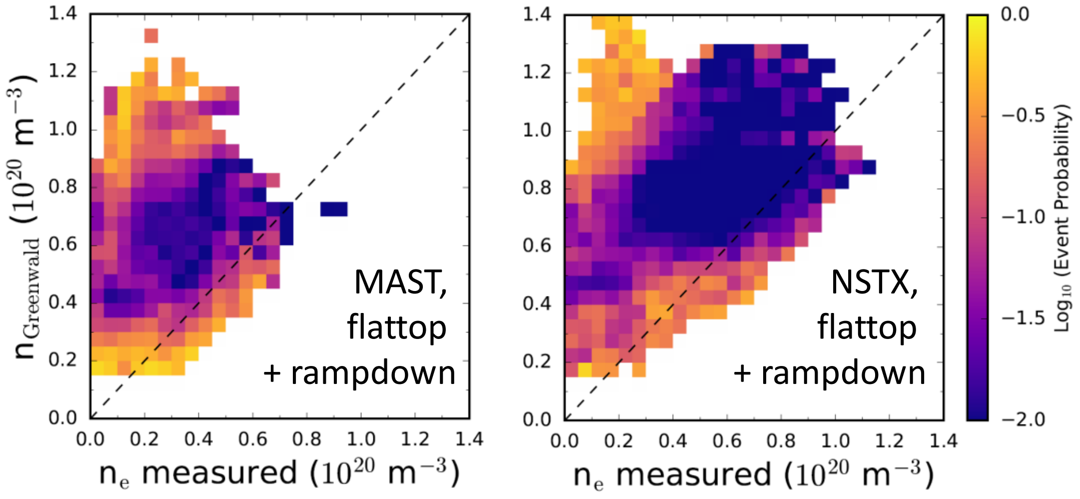

Figure 4: Disruptivity diagrams for the MAST and NSTX databases in the space of measured vs. Greenwald density, for times in the flattop and rampdown. Contours indicate the probability of disruption occurring in the database of plasmas in each section of parameter space.

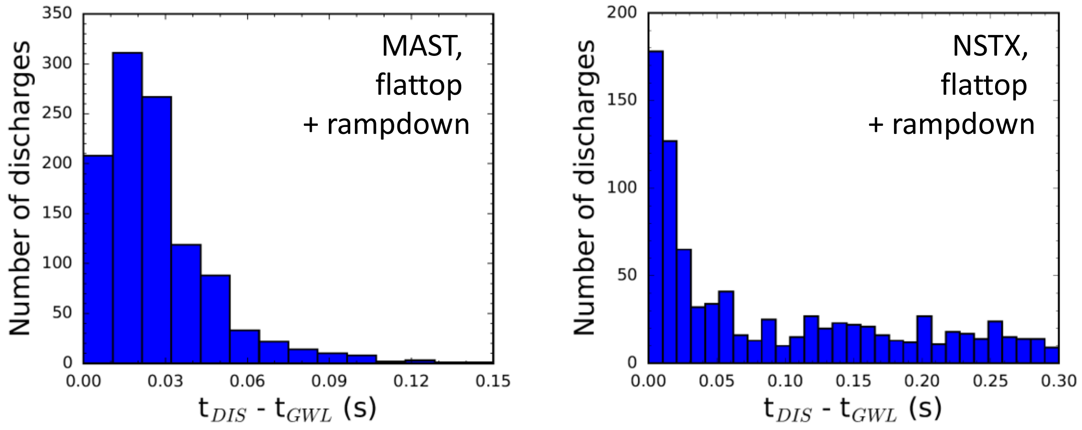

Figure 5: Histograms of MAST and NSTX discharges with both GWL and DIS events, showing the amount of warning time between the two. Note the different scales.

reconstructions were sampled at 10 ms and only times during the current flattop were considered (until section 3). Therefore a one second flattop provides 100 data points to the analysis, whereas a shorter shot, such as a MAST discharge with a 0.3 s flattop would only provide 30 points. Since each discharge can disrupt only (at most) once, machines with nominally shorter discharges will show larger disruptivity levels. In other words, disruptivity is measured on a per-time basis, not per-shot.

The diagrams are relatively similar for the two different machines, all showing the Greenwald limit as a rough guide to the operational limit of the machines, and all showing increased disruptivity along the line. Similar results have been shown in the past for other machines, for example JET [43]. Both MAST and NSTX are seen to be able to slightly exceed the Greenwald limit, which is consistent with previous results for MAST [48,49]. Disruptivity was previously seen to increase at values just over the Greenwald limit in NSTX as well [44].

It should be noted that disruptivity diagrams can be somewhat misleading, because they indicate the parameter space where the disruption finally occurs, not the point at which an event preceding the disruption where trouble begins occurs [20,24]. However, in the particular case of density limits in NSTX and MAST the results should not be too misleading because density tended to steadily increase in the discharges (see Fig. 1). This means that disruptions may occur slightly to the right on the figures of where the plasmas started to be in danger of collapse, which may contribute to the reason that the operational space crosses over the dashed line indicating the Greenwald limit.

3. Density limits in the rampdown

Generally, there are two ways in which a tokamak plasma can cross the Greenwald limit. Up until now we have been considering the first: when the density of a plasma rises high enough to cross a limit which is fairly steady in the flat-top current phase of a tokamak plasma (constant I_p and a). However, it has also been seen that during a plasma current ramp-down, the Greenwald limit can itself decrease, bringing the limit below the density. An example of this second mechanism from MAST is shown in Fig. 3.

As was mentioned for Figs. 1 and 2, another thing that can be seen in Fig. 3 is that spherical tokamak plasmas can exceed the Greenwald density to some degree before disruption. In fact, this was previously seen for MAST [49]. In Fig. 4 a repeat of the disruptivity diagrams in Fig. 2 is shown, now for the flat-top plus rampdown phases.

Including rampdowns adds 23,414 time points to the MAST database and 4,440 disruptions, essentially doubling the number of disruptions. Nearly all the 8,902 MAST discharges analysed disrupted in either the flattop or rampdown, a consequence of the mode of operation of the device. However, the increase in GWL events detected by DECAF is even more substantial when rampdowns are included. In fact, in the flattops of the 8,902 MAST discharges, it was quite rare for the GWL event to occur – only 115 such cases appeared, which is consistent with Fig. 2. An additional 1,000 occurrences appear in the rampdown. Similarly for NSTX, Fig. 4 shows considerably more rampdown disruptions above the Greenwald limit than Fig. 2.

Therefore when rampdowns are included, more disruptions over the Greenwald limit appear in the diagram, especially at lower levels of the limit (below $n_G \sim 0.5\times10^{20}\text{m}^{-3}$). This is evidence of disruptions occurring often when the limit is lowered during the rampdown. Note that when plasma current decreases at the same time that plasma density is increasing, movement in parameter space is diagonal from the upper left towards the lower right.

A real-time warning that would potentially occur at the dashed line for a disruption that eventually occurred over that line could provide some early warning time. Histograms of the times between DECAF events GWL and DIS (for the discharges when both occur: 1,115 total for MAST and 1,068 for NSTX) are shown in Fig. 5. One can see that, unfortunately, there is very often less than 30 ms between the GWL warning and the disruption. This is less warning time than some other signals can provide [52]. Of course, the warning level for GWL could be set to a Greenwald fraction below one, which would provide more time, but would limit plasmas to lower densities.

Rampdown density limit disruptions present a challenge because generally it is more difficult to decrease plasma density in a controlled manner than to increase it. Carefully tailored rampdowns are also necessary for future machines such as ITER [53,54] which will have a very large amount of potentially dangerous energy remaining in their plasmas even well into the rampdown.

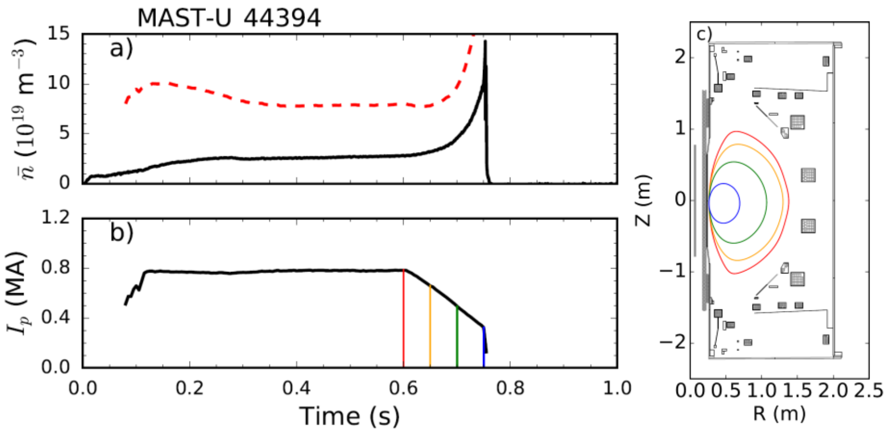

Figure 6: A MAST-U discharge that shrinks during the current rampdown and avoids the Greenwald limit (dashed red line). Four times during the rampdown are highlighted with different colors in frame b) and the corresponding plasma sizes are shown in frame c).

In NSTX-U [55], the upgrade to NSTX, neutral beam injection power was ramped down as the current was ramped down, causing the density to drop and keep the Greenwald fraction roughly constant [56]. Similarly, density control via gas valves is employed in MAST-U, as will be discussed later. Another possible strategy to avoid density limit disruptions in the rampdown if the density can not be decreased quickly enough, is to raise the limit itself by shrinking the plasma as the current decreases. While this may increase the density by compressing the plasma, it also increases the current density ($I_p/\pi a^2$ in the Greenwald limit). This strategy was recently successfully demonstrated in MAST-U in a discharge illustrated in Fig. 6. Further experiments to optimize the rampdown in MAST-U are planned, considering not only density limits but also vertical stability and more.

4. Local theories of the density limit

One advantage of the DECAF code is its modular approach, meaning that multiple theories and calculations for the density limit can be accommodated and tested, working towards finding which works best as a disruption predictor as well as seeing if elements of the theories can be confirmed. The straightforward Greenwald limit was trivially included in the first iterations of the DECAF code, but further exploration of density limit theories continues.

Some theories have attempted what essentially amounts to corrections to the Greenwald limit. For example, in Ref. [37], a power balance model was used to derive a density limit for tokamaks in low (L-mode) confinement, which ends up with a similar form to the Greenwald limit, but with an additional dependence on input power divided by plasma current. We attempted to implement a version of this expression, but it did not lead to any visible improvement over the Greenwald limit, for example in the disruptivity diagrams of Fig. 4. It should be noted, of course, that the databases are comprised not insignificantly of H-mode (high confinement) discharge time periods, whereas the theory was derived for L-mode.

Rather than continuing to test improvements to global density limit expression, however, another possibility will presently be explored. That is to consider the local physics conditions which underlie the global limits.

4.1 Local island power balance limit

One challenge of testing local limits that are more complex than the Greenwald limit is the availability of the necessary inputs in a large shot database. While the GWL event, which depends on having measured n_e, I_p, and a only was straightforward to calculate for large databases, as shown in sections 2 and 3, local limits may not be. Therefore the density event for NSTX was further tested with a limited set of thirteen discharges, as an illustrative example in Ref. [24]. Discharges were selected that had a long flat-top period of rising density and a period of no magnetohydrodynamic (MHD) activity until low frequency n = 1 activity appears with a clean signature in the spectrogram, that lasts less than 200 ms, and then the discharge terminates. This phenomenology was relatively common in NSTX. Localized tearing mode locking can often be one of the last events before disruption in tokamaks [28], but locked mode detectors may not give sufficient warning to avoid disruptions. Physics-based models of MHD mode slowing which have the potential for earlier warning of impending disruption have now been implemented in DECAF [20,21,22,23,24]. One potential complication, however, is that there is some evidence that these models of mode locking may not work optimally when the plasma is already near the density limit [57].

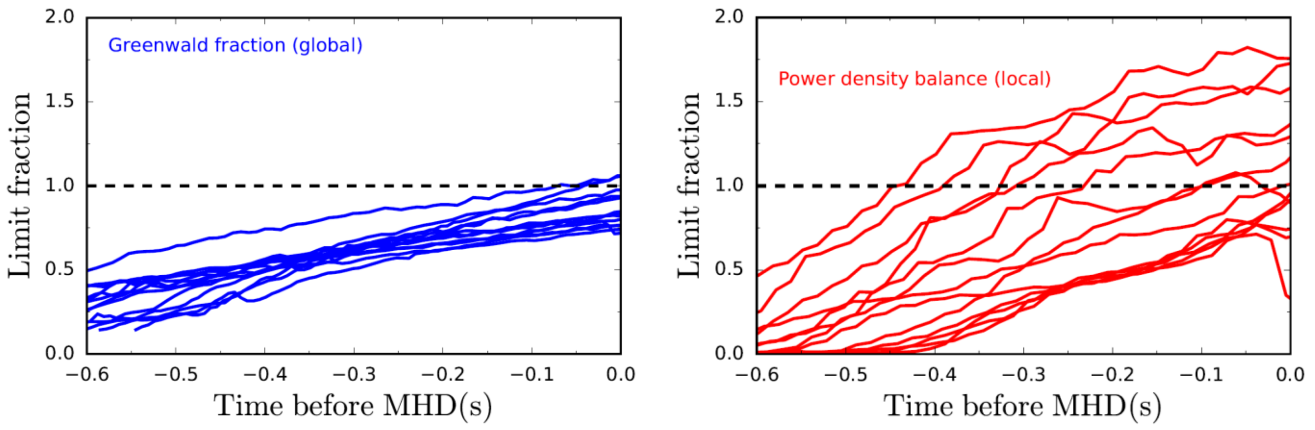

Figure 7: Greenwald fraction and local power limit fraction for 13 NSTX discharges vs. time leading up to the onset of low frequency MHD activity.

Additionally, however, density limits may be related to the onset of the MHD and therefore provide an early warning as well. Therefore the selected discharges were used to test a local island power balance limit theory [34]. This theory and its implementation in DECAF was explained in Refs. [20,24] and will not be repeated in detail here, but essentially it posits that there is a maximum local density at an island location that scales with local current density, resulting from a power balance between input Ohmic heating (P_{input}, calculated from resistivity and current density) and radiated power loss (P_{loss}, calculated from measured density and temperature profiles) [58].

In order to test this theory and implement it as a warning algorithm, the necessary inputs were imported to DECAF [20,24]. These include: the radiated power profile, the resistivity profile, and the current density profile from the TRANSP code [59]. The latter was an expansion of DECAF capability as previously no external code had been used to import calculated quantities (besides those from equilibrium reconstructions). This represents an opportunity but one that must be used cautiously as TRANSP calculations are not universally available for database studies, nor will they be in future real-time applications (we will return to this point in section 5).

The power balance criteria was presented as a limit in DECAF and the event called IPB for island power balance. The calculation was performed locally at the q = 2 surface because m/n = 2/1 activity is the most likely candidate for MHD activity and island growth. This presented a challenge, however, because while equilibrium reconstructions (magnetics only, or partial kinetic, including in real-time) can give a radius of the q = 2 surface, it usually has some error and is somewhat noisy in time, which means the resulting calculated power limit fraction can also be noisy. To combat this, we approximated the radius of the q = 2 surface as a smooth, linear function in time during the discharge (usually increasing slightly in time). For each discharge this function was determined from the noisier post-discharge equilibrium reconstructed location, which means that our evaluation of this data set is not set up at present for real-time application, but one could imagine using a prescribed q = 2 location for a planned discharge or a moving average from real-time equilibrium reconstruction. This also means that the calculation is not necessarily exactly local to the island location, though it should be quite close. Additional assumptions of the present model evaluation include the TRANSP calculation of the current density, which is surface averaged and also performed a posteriori, and the assumption that carbon is the only impurity. Future improvements of the model implementation are possible.

Nevertheless, the model was applied to the aforementioned set of 13 NSTX discharges, and the results, of P_{loss}/P_{input} vs. time leading up to the time of the end of shot MHD onset, are shown in Fig. 7. One example had previously been shown in more detail in Ref. [24].

It should be mentioned that there were also other discharges attempted for this calculation that are not shown in which the model failed to give reasonable results, whether through lack of good data or potential errors from the assumptions mentioned above. The model could be run on many thousands of more discharges from the DECAF database than are shown here, but as can be seen in Fig. 7, it needs improvement before that would be a useful exercise.

Also shown in Fig. 7 are the Greenwald fractions for each discharge. One can see that, because of the rising density in these discharges, both criteria tend to rise with time towards the end of the discharge, towards, or surpassing, the theoretical limit of unity. The criteria are obviously correlated since both depend on the rising density, but it is clear that the Greenwald limit is presently a good deal more consistent than the local power balance model. The Greenwald fraction has a range of about 0.75 to 1.05 at the time of MHD onset, and actually somewhat higher at the time of disruption which comes within a few hundred milliseconds thereafter, while the power limit fraction has a range of about 0.60 to 1.65. This is not really surprising, with the Greenwald limit being a global calculation, while the power balance calculation is a local one with all the potential error that entails. Further work is required, then, to determine both whether the local power balance model represents a good physical explanation for the Greenwald limit, and whether it is a useful criterion to monitor for disruption avoidance purposes. While the goal is not to attain perfection in the model for forecasting purposes, but rather usefulness, it is clear that for the present, the global Greenwald limit is shown to still be more useful for these purposes.

4.2 A note on the connection between density and radiative limits

One major limitation of the simplicity of our implementation of the local island power balance model is that only carbon was considered there, whereas in reality very small quantities of high Z materials, such as iron, could potentially have a large impact [58]. Other limitations are that the impurity radiation processes in tokamak plasmas can be more complex than was accounted for by simple formulae [60]. However, the authors of the theory claim that its relative simplicity is beneficial as it compactly explains the connection between radiative collapse and the density limit, and the density limit's lack of or weak dependence on heating power, effective ion charge Z_{eff}, plasma shaping, and safety factor q [34]. There are, of course, alternative theories that could be explored, such as one also derived from radiation balance and related to MARFEs [61] that results in a similar expression for density, although with a term proportional to the square root of the auxiliary heating power [62].

As with most of the theories, the local island power balance limit described in section 4.1 in many ways illustrates the connection between density limits and radiative limits. This, and the next three described, all involve a local power balance, where the radiated power P_{rad} can be a key component. A simple comparison that has been identified as a potentially useful disruption warning signal is the ratio of radiated power to input heating power [52,63]. A global balance of radiative power vs. input power might be more consistent as a forecaster in the way that was shown for density in Fig. 7. Also if this calculated radiated power quantity, based on density and temperature measurements, could be shown to be comparable to the measured quantity, then the method could be used to forecast the radiated power in tokamaks without a real-time bolometry systems, or to predict it based on estimates of those measurements.

In some cases in NSTX, the concentration of iron in the plasma was seen to rise very significantly in the plasma after a radiative collapse. Such occurrences have been observed in many devices, such as JET [64] and Alcator C-Mod [65], and can have different causes, with one particularly troublesome one being debris falling into the plasma. Very little warning time is available sometimes with radiated power spikes. Nevertheless, it is possible for plasmas that experience thermal quenches due to impurity radiation influxes to recover and avoid current quenches, either naturally [64] or possibly by application of lower hybrid waves [65].

The potential for disruption due to radiative collapse, but especially the potential for avoiding those disruptions motivates the identification and understanding of these events. A second test monitoring the radiated power time rate of change could also be made available, which would compliment the threshold test on the radiative power fraction. Additionally, the peaking factor for radiation profile was considered in Ref. [12].

4.3 Ballooning stability at the separatrix

In Ref. [36], Eich et. al demonstrated that for JET and AUG plasmas there is a correlation between the Greenwald limit and the ideal ballooning instability threshold at the separatrix, pointing to ballooning stability possibly being the underlying cause of the density limit.

Like the previous subsection, this theory transforms the global limit into a potentially testable local criterion, in this case at the separatrix. The required inputs are geometric factors such as the major radius R, minor radius a, and the elongation κ, as well the toroidal field B_t, and the total power crossing the separatrix, $P_{sep} = P_{heat} - P_{rad}$, where P_{heat} is the total heating power from Ohmic and external sources. Further specifics of these power quantities will be discussed further in section 5.

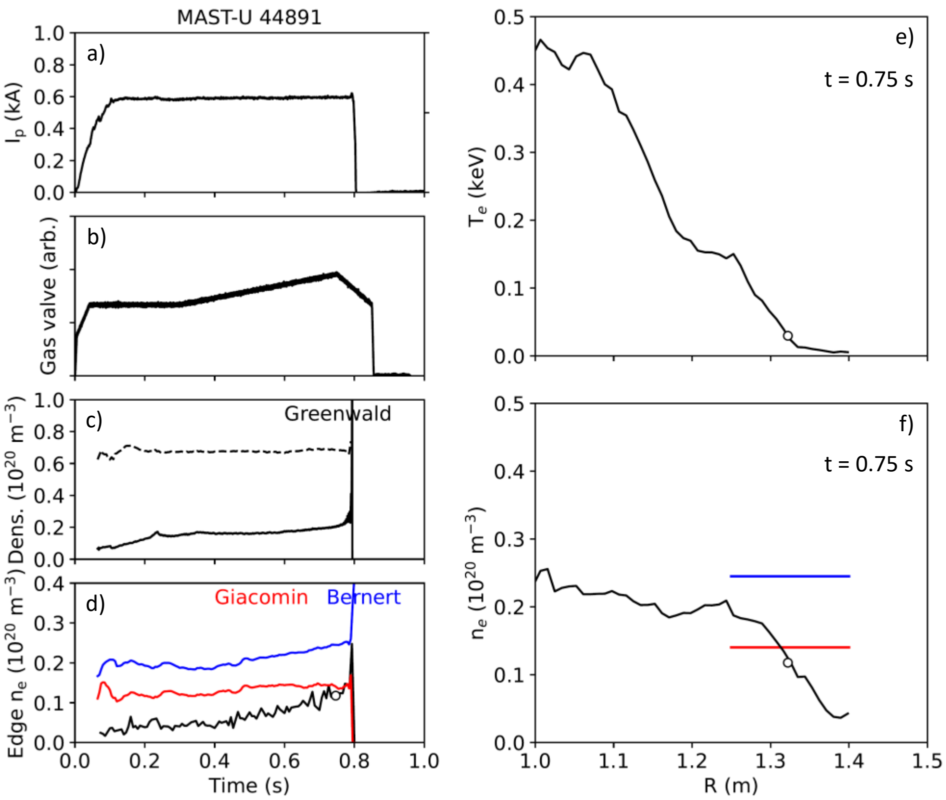

Figure 8: Quantities from MAST-U discharge 44891, including: a) plasma current, b) gas valve voltage, c) measured line averaged density and calculated Greenwald density, d) edge density compared to two local limits, e) and profiles of electron temperature and f) density at the time indicated by a marker in d).

From these the electron temperature at the separatrix is determined which gives R_{sep} on a Thomson scattering measurement profile, and therefore $n_{e,sep}$.

$$T_{e,sep} \approx \left(\frac{7P_{sep}q_{cyl}^{2}A}{16\kappa_0^e\hat{\kappa}\langle\lambda_q\rangle}\right)^{\frac{2}{7}}, \qquad (1)$$

where q_{cyl} is the cylindrical safety factor, $A = R/a$, $\kappa_0^e = 2000$ $(\text{eV})^{-7/2}$ Wm^{-1} is the Spitzer-Harm electron heat conduction constant, $\hat{\kappa} = ((1+\kappa_{geo}{}^2)/2)^{-0.5}$, and λ_q is the power decay length at the separatrix.

Then a critical separatrix density is derived in Ref. [36] from ballooning stability:

$$n_{e,sep}^{crit} = \left(\frac{1+\kappa_{geo}{}^2}{2}\right)^{\frac{2}{7}} \frac{B_t^2}{P_{sep}^{2/7}\cdot R\cdot q_{cyl}^{18/7}}\cdot\langle\lambda_q\rangle^{\frac{9}{7}}. \qquad (2)$$

This expression was evaluated for its usefulness for spherical tokamaks, but two issues were seen. First, the derivation relies on some approximations that lead, for example, to using the cylindrical safety factor. Second, the power decay length, λ_q, scaling used in Ref. [36] was for AUG and JET; when updated for STs [66], it was found that this made the calculated n^{crit} very large. Interestingly, the scaling for MAST in Ref. [66] where $\lambda_q \sim P_{sep}{}^{2/9}$ exactly eliminates the dependence of $n_{e,sep}^{crit}$ on P_{sep}. Ultimately, it was decided that at this time further theory development would be needed to use this local density limit criterion for STs.

4.4 Empirical critical edge line density

A recent empirical critical edge line density from Bernert et al. [31] has found some success for the AUG [28,32,67] and TCV [33] devices. The fairly straightforwardly computed limit was intended to describe the various phases of the H-mode density limit [28]. In its original form it was an edge line density limit specific to a particular AUG chord located at around 0.7 *r/a*, but it was later extended to TCV, re-scaled for the different geometry. This indicates that this Bernert limit may be useful more generally as edge density limit, perhaps with change in constant. The critical line density is given by:

$$n_{e,crit} = 0.506\cdot\frac{P_{heat}^{0.396}\cdot I_p^{0.265}}{q_{95}^{0.323}}, \qquad (3)$$

where q_{95} is the safety factor at the 95% flux surface. This was then implemented for AUG and TCV as an area of high

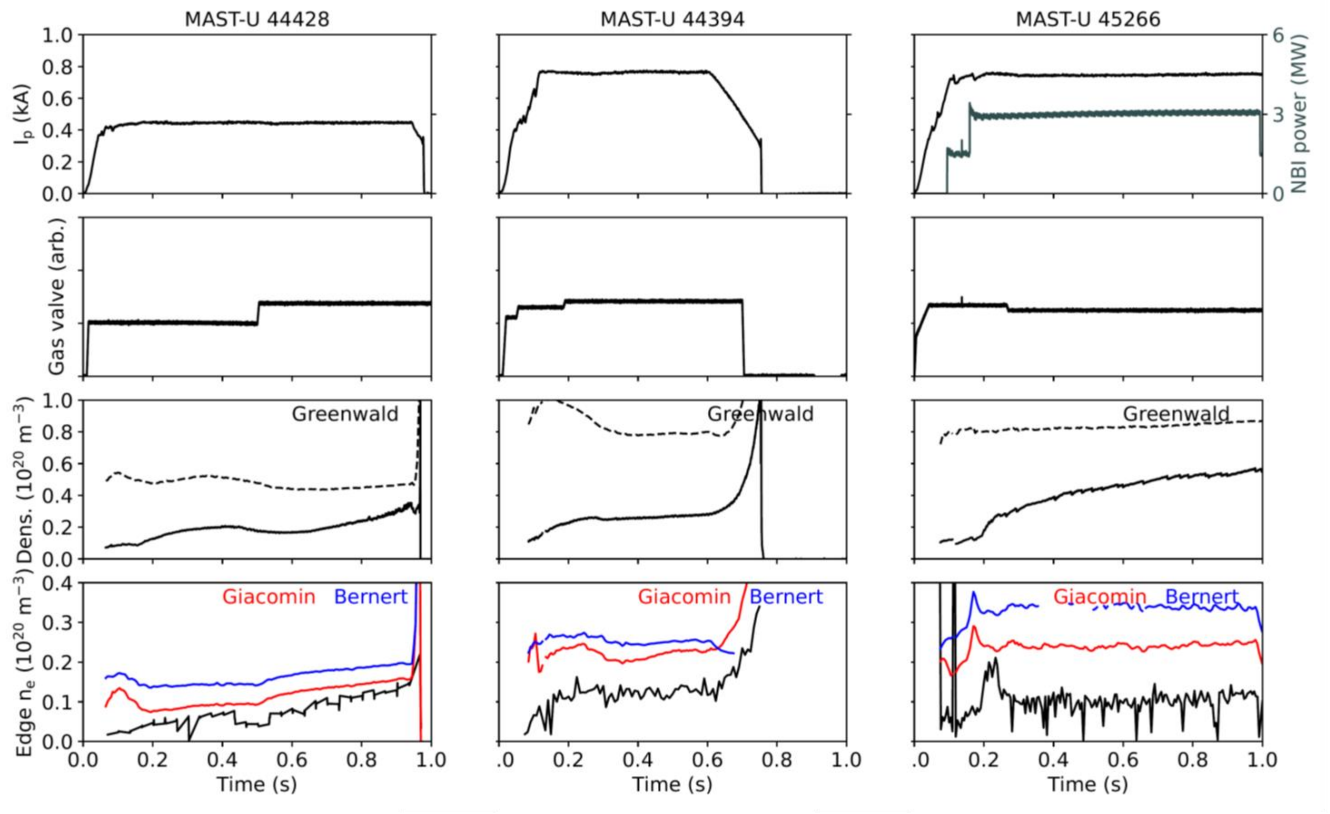

Figure 9: Plots for three MAST-U discharges of plasma current (and NBI power for the third), gas valve voltage, measured line averaged density and calculated Greenwald density, and edge density compared to two local limits.

$n_e/n_{e,crit}$ vs. low $H_{98y,2}$ space to be avoided. It should be noted that the area of parameter space to be avoided was defined not by where the disruptions occurred, but rather where the high to low-confinement, H to L, back transitions occurred in the phase leading to disruption [67]. Here $H_{98y,2}$ is the energy confinement time scaling factor [68,69]. This type of plot is similar to more common H_{98y2} vs. n/n_{GW} plots [51,70,71,72] where n is either line density or sometimes scrape-off layer density, and the Greenwald normalization is of course different from the $n_{e,crit}$ used here.

We have implemented this capability in DECAF, using inputs from measured density, equilibrium reconstruction, and the TRANSP code for $H_{98y,2}$ and P_{heat}. This capability can be used for any of the many machines that DECAF can read data from. Indeed, the calculation in DECAF was verified by first applying it to the same AUG discharges shown in Ref. [28], and obtaining the same published results. However, here it was further tested for STs by using a set of MAST-U discharges that probed the density limit.

It was previously noted that MAST-U, for the most part, has operated under the Greenwald limit. Nevertheless, in an albeit limited set of discharges so far, rising density appears to have sometimes caused disruptions at levels below the Greenwald limit. This, and the availability of very detailed density profile measurements from MAST-U's world-leading Thomson scattering diagnostic [73] make it a good platform to test these new edge density limit theories for spherical tokamaks.

First, the edge density level to be compared to the critical level must be defined. Unlike in AUG with a dedicated chord for a line density measurement, here we use the measured electron density at the separatrix. This somewhat stretches the original intention of the limit, but we are interested in testing its general applicability. The separatrix position was found by calculating the expected edge temperature from Eq. (1), using that to find R_{sep}, and therefore $n_{e,sep}$ in the radially detailed Thomson scattering profiles for MAST-U.

As an example, MAST-U discharge 44891 is shown in Fig. 8. In a) the plasma current shows an abrupt disruption at about 0.8 s. In this discharge the gas valve voltage was continually increased (b), leading to a steady increase in line averaged density (c) that nevertheless was well below the Greenwald density. The separatrix density is also below the Bernert limit of Eq. (3) in panel (d) (the Giacomin limit will be discussed in the next subsection). The Thomson profiles of T_e and n_e are shown in (e) and (f) for a time ~ 0.75 s near the end of the discharge. In these profiles, the $T_{e,sep}$ from Eq. (1) of about 30 eV gives an R_{sep} of about 1.32 m. The $n_{e,sep}$ value at that location is indicated on the density profile in (f).

In general, without a change in constant, we found that the Bernert limit was usually above the achieved edge density values that were analyzed here. Perhaps with further investigation of the disruptive boundary in the $n_e/n_{e,crit}$ vs. $H_{98y,2}$ space, and with subsequent adjustment for the particular machine being considered, the Bernert limit could prove generally useful. More cases, and more discussion of the Bernert limit, will be shown in the next subsection, in conjunction with the final edge limit explored in this paper which displays, as will be seen, similar dependencies.

It must be noted that the Bernert limit was implemented in real-time control systems already at AUG [32,67] and TCV [33,74]. In the TCV case, for example, various levels (constants in Eq. 3) were used to activate different actuators. First, the gas voltage increase was stopped in an effort to stop increasing density. When the plasma continued further into the dangerous zone in the $n_e/n_{e,crit}$ vs. $H_{98y,2}$ plot, the heating power was increased in an effort to move the limit.

4.5 Boundary turbulent transport

Giacomin et al. [38] studied the phase following an H to L back transition and MARFE onset in plasmas. They found that increasing density at the separatrix leads to increased collisionality and turbulent transport until there is a loss of power balance between heating and turbulence, which causes a collapse. The derivation will not be described here, but it leads to a local edge density limit given by:

$$n_{e,crit} = \alpha A^{1/6} a^{3/14} P_{sep}^{10/21} R^{-43/42} q_{95}^{-22/21} (1 + \kappa^2)^{-1/3} B_t^{2/3}, \quad (4)$$

where α is a numerical coefficient, which we have taken to be 3.3 as in Ref. [38]. This limit has also now been implemented in DECAF, with all necessary quantities coming from equilibrium reconstruction except P_{sep} which is obtained from TRANSP.

The Giacomin limit is calculated at all times of the discharge despite being derived specifically for the post H to L transition period. Once again we may therefore be stretching the original intent of the theory somewhat, but again the goal is to evaluate its general applicability. It should be noted that H to L back transition detection could be automated [63], and is indeed currently being implemented in DECAF.

The previously discussed Fig. 8(d) also contains the Giacomin limit, where it can be seen that the Giacomin limit is somewhat lower than the Bernert limit. We found this to generally be the case for MAST-U.

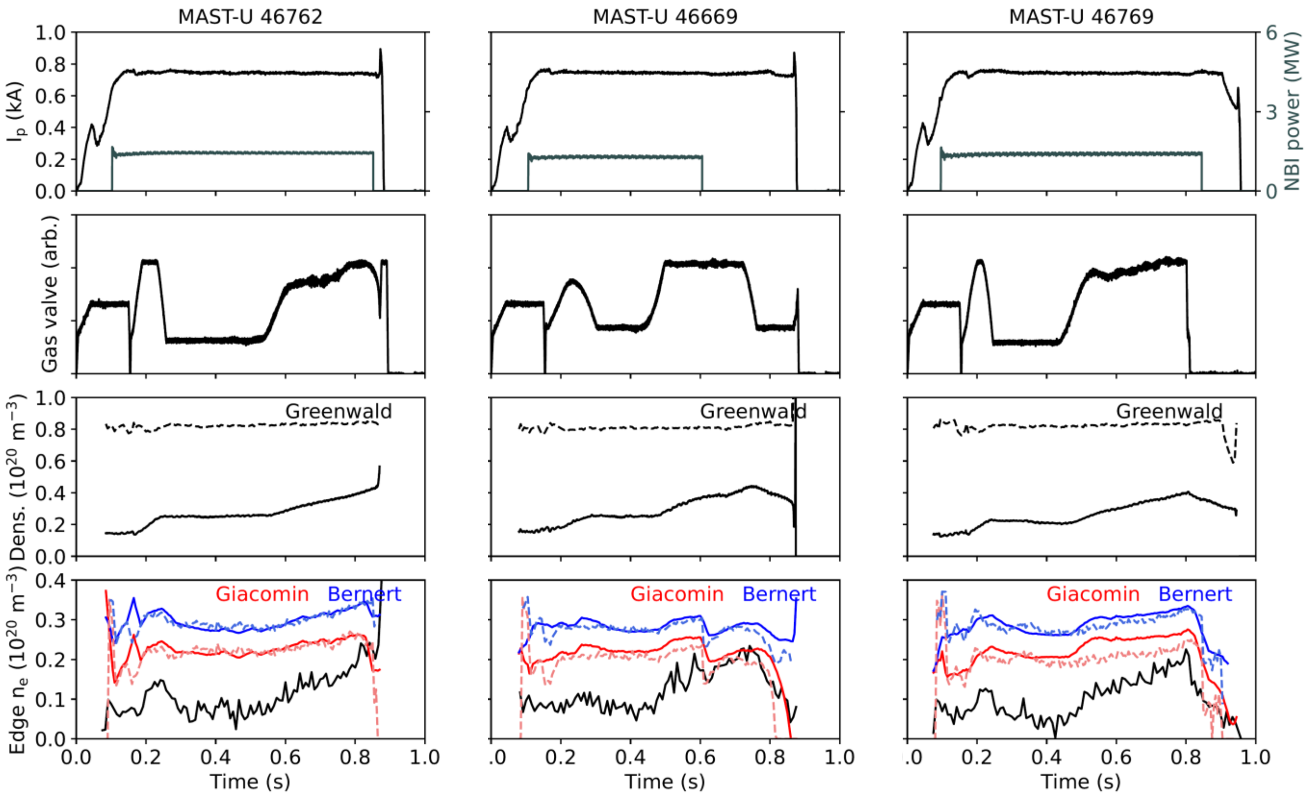

Figure 10: Plots for three MAST-U discharges of plasma current and NBI power, gas valve voltage, measured line averaged density and calculated Greenwald density, and edge density compared to two local limits. The lighter, dashed lines are made using proxies for TRANSP quantities, as explained in section 5.

The Bernert and Giacomin limits will now be compared generally for a range of MAST-U plasma conditions. Note that because the Greenwald limit scales with I_p (the range of a values is fairly small), the Greenwald limit changes by almost a factor of two from 400 kA plasmas to 750 kA. All else being equal, one would expect from Eq. (3) that the Bernert limit would only increase by 18% due to that range of I_p increase, and from Eq. (4) that the Giacomin limit would not increase at all. Of course rarely, if ever, do no other parameters change.

For a real world example, in Fig. 9 we contrast three MAST-U discharges: 44428 (Ohmically-heated at 400 kA), 44394 (Ohmically-heated at 750 kA), and 45266 (two-beam heated at 750 kA). All have fairly similar gas valve voltages, and the Greenwald limit behavior is as expected - proportionally higher in the 750 kA discharges. However, the edge density limits have both risen between each shot. The Bernert limit rises steadily between the cases, mostly due to the heating power rising from 400 kA to 750 kA and then from Ohmic to two-beam. The change in I_p and a small decrease in q_{95} between the first two cases (from ~7.7 to ~5.2) only contribute modestly to the difference. Note that the times with a gap in the Bernert limit line in the third case is a time period when $H_{98y,2} > 1$.

The Giacomin limit rises substantially between the 400 kA case and the 750 kA Ohmic case, despite having no explicit dependence on I_p, and then modestly again in the two-beam case. This comes primarily, again, from the rise in heating power, but the change in q_{95} this time has more effect – helping to increase the limit as q_{95} drops between the first and second case, and working against the heating power as q_{95} increased slightly (to ~6.1) between the second and third cases.

For each discharge, the limits are all fairly steady with time because the plasma conditions were held constant in the flattop. The exception is in 44394 when the plasma current goes into a rampdown and the Greenwald limit *increases* despite n_G being proportional to I_p. This is because in this particular case the plasma was shrunk in the rampdown (see Fig. 6), decreasing a and κ and q_{95}. The rate of shape change was enough to increase the Greenwald and Giacomin limits, but the I_p and q_{95} decreases largely offset in the Bernert limit.

The heating power is an obvious input to both edge density limits and a natural test would be to increase beam heating power systematically in discharges with rising density to see if higher edge density can then be safely accommodated in the shots as predicted by the rising limits. With enough test cases, the effect of q_{95} might be separated out as well. Unfortunately in the first MAST-U campaigns the majority of intentional density ramps (of which there were not many) were performed in lower current, Ohmic plasmas. A more systematic exploration of the effect of heating on density limits may be performed in future MAST-U campaigns.

There do exist, however, some discharges in MAST-U that provide a natural experiment, of sorts, on the effect of input power on the edge density limits. A second illustration, Fig. 10, shows three MAST-U discharges with I_p ~ 750 kA and neutral beam injection (NBI) from one of the two MAST-U beams. In each case the NBI provides a steady power until a time in the flattop when it is suddenly turned off and consequently the edge density limits also suddenly drop. At this point in the MAST-U experimental campaign, density control with the gas valves was being implemented and so various, more complex gas valve voltage evolutions are evident in these shots. When the drop of NBI power and edge limits corresponds to a still increasing density, as in the first case, 46762, the Giacomin limit is suddenly passed and a disruption occurs. In the second case, 46669, the experimental density barely skirts under the limit (actually very slightly crosses) until the gas valve voltage is turned down and the density drops, staying below the limit until a later, lower time when a disruption does occur, but it is not clear this is due to a density limit in this case. Finally, in the third case, 46769, the gas valve voltage happens to be turned off before the NBI power is lost, so the density decreases and stays below the limits throughout the rest of the flattop and into the rampdown.

Before further controlled experiments can be performed, the best test of the effectiveness of the edge density limits in MAST-U is to analyze together all of the handfuls of discharges with density ramps in different plasma conditions. These are the Ohmic shots at ~400 kA (44226, 44227, 44428 (shown in Fig. 9), 44604, and 44605) which mostly don't disrupt, the Ohmic shots at ~600 kA (44891 (shown in Fig. 8), 44892, 44904, and 44905) which all do cross the lower Giacomin limit at least, and all disrupt, and the just discussed ~750 kA, one beam discharges (46669, 46762, 46769 in Fig. 10, plus two others 46671, 46672 for comparison).

These cases are now all illustrated in Fig. 11, in which for each shot the time evolution of the measured line density divided by the Greenwald density is shown on the y-axis, and the measured edge density divided by the Giacomin limit is shown on the x-axis. Disruptions are marked by stars and they all occur over, or near, the Giacomin limit.

In the 400 kA cases, 44604 crosses well over the Giacomin limit and then (barely) the Greenwald limit, collapses, partially recovers, and then disrupts. Discharge 44227 does not disrupt despite crossing both limits. The density limit determination is not particularly successful, then, in this small set of low current Ohmic discharges.

In all cases, but especially in the higher current discharges where the Greenwald limit is larger, the trajectory of density rise in these plasmas is to cross the edge density limit when the global density only reaches about half of the limit. Note also that all the higher current discharges never actually cross the Greenwald limit.

In the middle 600 kA cases of Fig. 11, the disruptions occur near the Giacomin limit. Discharge 44904 actually crosses the limit before disrupting under it (the smoothing used in the plot takes out a single time point spike over the limit). In contrast, the trajectory of discharge 44892 appears to go off the edge of the plot before the disruption, but this was actually due to a temporary loss of the Thomson scattering edge channels and the algorithm defaulting to the last measured channel which was farther in the plasma and therefore at higher density. This serves to illustrate one potential difficulty of a true real-time system monitoring these signals. Overall the 600 kA cases perform well with respect to the Giacomin limit, though.

Similarly the 750 kA beam heated cases perform well as well, with the discharges that stay below the limit not disrupting and the ones that cross disrupting soon after.

Clearly this analysis represents a limited test of the effectiveness of the edge limits in forecasting disruptions, but it does seem to perform fairly well, except perhaps in the ~400 kA case, with the discharges that stay under the edge limit not disrupting and those that do cross for the most part disrupting near the limit. Overall this analysis shows that there could be potential for edge limits to give an early warning that would not be picked up by a disruption warning system merely monitoring the global Greenwald limit.

5. Discussion of applicability of edge density limits as real-time disruption indicators

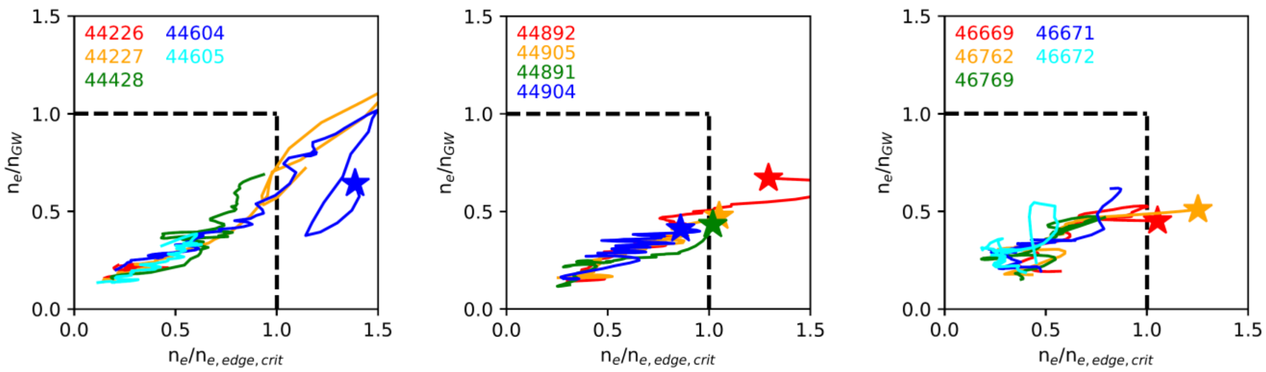

Figure 11: Plots of $n_e/n_{e,crit}$ vs. n_e/n_{GW} for (left) five MAST-U Ohmic ~400 kA discharges, (middle) four Ohmic ~600 kA discharges, and (right) five beam heated ~750 kA discharges. Stars indicate disruptions.

The traces in Fig. 11 have been smoothed in time for clarity of presentation. It is evident from the bottom panels of Figs. 9 and 10 that the edge density measurement is a noisy signal. This is due to the method of determining $T_{e,sep}$ to get R_{sep} to get $n_{e,sep}$ illustrated in Fig. 8, as well as noise in the measured Thomson n_e profile itself. Naturally, the line integrated measurement used in the Greenwald limit and the global quantities in the simple limit calculation lend themselves to smoother evaluation. This is the same issue as was seen in section 4.4 however it appears somewhat less pronounced trying to localize edge measurements rather than local $q = 2$ surface quantities from calculated profiles.

One potential consequence of noisy signals, however, is false positives. The Giacomin limit was never intended to be taken as a stringent, binary limit demarcating a disruptive/non-disruptive boundary (in Ref. [38] there is spread in the comparison of the derived limit to data from different machines). However, even as a warning signal, false warnings would occur when spurious crossings of the limit happen (see, for example, in Fig. 10(d) for 46669). Smoothing the measured signals in time, as done for Fig. 11, might help, but it introduces a time delay to the warning. Another strategy is for the warning system to require the measurement to stay above the limit for a certain amount of time before declaring a warning; again this introduces a delay.

The Giacomin limit was used here because it was found to always be smaller than the Bernert limit for MAST-U. Recall, however, that the "edge" density was measured at about 0.7 r/a in the original implementation for AUG, so the measured density in that case should be subsequently higher. In the future if the Bernert limit is to be used in a disruption warning system, it should be scaled for each particular machine. Here, for the very limited cases shown, it seems that MAST-U would require a factor of ~0.7, which would bring the Bernert limit very much in line with the Giacomin limit. Much more data would be required to truly determine this, however.

In the end we are interested in the edge density limits not just for their possibility to explain the physics of the density limit, but also for their potential utility, alongside the established Greenwald limit, for use as disruption indicators in a real-time system.

There are three factors now to consider: the real-time measurement of edge density, the real-time calculation of critical edge density, and the response of the actuator in a density control system.

First, there are varying degrees of complication to the measurement of real-time edge density. As was mentioned previously, in the AUG real-time experimental case a single dedicated edge chord was used for a measured edge line density. Here we used a post-processing technique of evaluating edge T_e from Eq. (1) and finding the n_e at the same radius from a detailed Thomson profile measurement. One can imagine the former technique perhaps being too simple (a plasma where the edge radius moves in time would effectively move the chord of the measurement), while the latter may be too complicated. Assuming detailed edge measured T_e and n_e profiles are available, though, a good compromise may be to select a constant value for T_e and thereby select the corresponding n_e, bypassing Eq. (1). We have tested this with T_e = 35 eV for the discharges in Fig. 10 and the edge density is virtually indistinguishable from what is plotted there.

The second side of the equation is the real-time evaluation of the critical edge density. Too complicated formulae, such as for example Eq. 19 in [75], probably don't stand much chance of simple assessment in real-time for a disruption warning system, but the Bernert and Giacomin limits discussed here do. Besides the $H_{98y,2}$ factor (essentially just used to determine the applicability of the Bernert limit), both limits evaluated here rely only on an equilibrium reconstruction except for the Bernert limit requiring P_{heat}, and the Giacomin limit requiring P_{sep} (= $P_{heat} - P_{rad}$). As was mentioned, we obtained both of these quantities from TRANSP, but an available real-time transport evaluation is probably best not to be assumed. Therefore, it is useful to evaluate the impact of using proxies for these quantities.

First, if measured P_{rad} from experimental bolometry signals, is trustworthy and available in real-time this would be the preferred quantity. If it is not but measured density and temperature profiles are, the method of calculating P_{loss} profiles used in the local island power balance calculation in section 4.1 could be expanded and used. The calculation performed there for NSTX was localized to the location of a magnetic island, but in actuality, the calculated P_{loss} profile [58] could also be projected on the 2D cross section of the plasma [76] and integrated toroidally for a total P_{rad} signal.

The P_{heat} quantity used here is the Ohmic heating power plus the total fast ion heating. The Ohmic power can be fairly well estimated by the loop voltage times the plasma current, or $P_{ohm} = -2\pi(d\psi_{bdy}/dt)*I_p$, quantities available from the equilibrium reconstruction.

The last piece is where TRANSP is truly useful, as the total fast ion heating is the injected NBI heating power P_{inj} minus orbit losses, charge exchange losses, and shine-through. All of these are dependent on the particulars of the NBI system and the plasma conditions. However, one could also here make an approximation. Generally, the NBI losses are inversely proportional to the density of the plasma, and we have found that for the MAST-U cases shown in Fig. 10, at least, $P_{heat} = -2\pi(d\psi_{bdy}/dt)*I_p + P_{inj} - 1\text{e}10^{20}\text{m}^{-3}/n_e$, provides a good rough estimate of the heating power. Using this for P_{heat} in the Bernert limit and subtracting the available measured P_{rad} (which does differ somewhat from the TRANSP P_{rad}) for the Giacomin limit we find the limit quantities plotted in Fig. 10(d) with the dashed lines. Generally, with some exception, these potentially more real-time calculable limits are quite close to the ones using TRANSP analysis. Again, a much larger study would be necessary to truly evaluate their effectiveness, however.

Finally, in the example of MAST-U, though the gas valves were not controlled in real-time as a response to the measured edge density approaching the edge density limits, the examples in Fig. 10(d) do provide examples of what the response might have been if they were. One can see that if an appropriate level of $n_e/n_{e,crit}$ was set as a warning level triggering the gas valves to shut off, or at least lower, the response of the edge density, though not immediate, is fast enough to potentially avoid disruption.

6. Conclusions

The tests of various density limit theories presented here are essentially first steps towards creating a more comprehensive model that can accurately warn of impending density limit disruptions. This may involve the use of various models together as input signals to a larger warning system, and will certainly require testing of those models on the larger DECAF databases of discharges from many devices. Additionally, a more generalized energy balance model that could “plug in” different transport assumptions could be needed to provide DECAF with the best model for forecasting and avoidance of these disruptions. This is a larger project left for future work.

Here we have shown that the global Greenwald limit, easily implemented in DECAF, does correlate with disruptions in the NSTX and MAST databases, and particularly in rampdowns. Local edge denity limits were also implemented and tested. The local island power balance model revealed some difficulties with noisiness of local assessment. The empirical Bernert and boundary turbulent transport Giacomin limits show good promise when tested vs. a limited set of MAST-U discharges, however,

Acknowledgements

The authors acknowledge helpful discussions with Alessandro Pau and Jack Lovell.

The digital data for this paper can be found in: XXX

This work was supported by the U.S. Department of Energy under contract numbers DE-AC02-09CH11466 and DE-SC0018623. The United States Government retains a non-exclusive, paid-up, irrevocable, world-wide license to publish or reproduce the published form of this manuscript, or allow others to do so, for United States Government purposes.

This work has been carried out within the framework of the EUROfusion Consortium, funded by the European Union via the Euratom Research and Training Programme (Grant Agreement No 101052200 — EUROfusion). Views and opinions expressed are however those of the author(s) only and do not necessarily reflect those of the European Union or the European Commission. Neither the European Union nor the European Commission can be held responsible for them. This work has also been funded by the EPSRC [grant number EP/T012250/1] and the EPSRC Energy Programme [grant number EP/W006839/1].

References

---

[1] M. Greenwald et al., Nuclear Fusion **28**, 2199 (1988)
[2] M. Greenwald, Plasma Physics and Controlled Fusion **44**, R27 (2002)
[3] T. C. Hender et al., Physics of Plasmas **6**, 1958 (1999)
[4] B. Lipschultz, Journal of Nuclear Materials **145-147**, 15 (1987)
[5] F. Felici et al., Proceedings of the IAEA Fusion Energy Conference 2016 pp EX/P8–33.
[6] T. C. Blanken et al., Fusion Engineering and Design **126**, 87 (2018)
[7] T. C. Blanken et al., Nucl. Fusion **59**, 026017 (2019)
[8] F. Pastore et al., Fusion Engineering and Design **192**, 113615 (2023)
[9] P. T. Lang et al., Nucl. Fusion **58**, 036001 (2018)
[10] O. Kudlacek et al., Fusion Engineering and Design **159**, 111735 (2020)
[11] A. Sengupta et al., Nucl. Fusion **41**, 487 (2001)
[12] W. Zheng et al., Nucl. Fusion **58**, 056016 (2018)
[13] C. Shen et al., Nucl. Fusion **63**, 046024 (2023)
[14] K. Zhang et al., Plasma Sci. Technol. **22**, 115602 (2020)
[15] W. H. Hu et al., Nucl. Fusion **61**, 066034 (2021)
[16] K. J. Montes et al., Nucl. Fusion **59**, 096015 (2019)
[17] J. X. Zhu et al., Nucl. Fusion **63**, 046009 (2023)
[18] C. Rea et al., Nucl. Fusion **59**, 096016 (2019)
[19] J. W. Berkery et al., Physics of Plasmas **24**, 056103 (2017)
[20] S. A. Sabbagh et al., Proceedings of the IAEA Fusion Energy Conference 2018 pp EX/P6-26.
[21] S. M. Kaye et al., Nucl. Fusion **59**, 112007 (2019)
[22] E. J. Strait et al., Nucl. Fusion **59**, 112012 (2019)
[23] S. A. Sabbagh et al., 2021 Proc. 28th Int. Conf. on Fusion Energy (2021)
[24] S. A. Sabbagh et al., Physics of Plasmas **30**, 032506 (2023)
[25] M Ono et al., Nucl. Fusion **40** 557 (2000)
[26] A Sykes et al., Nucl. Fusion **41** 1423 (2001)
[27] M. Kong et al., Nucl. Fusion **59**, 076035 (2019)
[28] M. Maraschek et al., Plasma Physics and Controlled Fusion **60**, 014047 (2018)
[29] U. Stroth et al., Nucl. Fusion **62**, 076008 (2021)
[30] T. Long et al., Nucl. Fusion **61**, 126066 (2021)
[31] M. Bernert et al., Plasma Phys. Control. Fusion **57**, 014038 (2015)
[32] B. Sieglin et al., Fusion Eng. And Design **161**, 111958 (2020)
[33] T. Vu et al., IEEE Trans. on Nucl. Sci. **68**, 1855 (2021)
[34] D. A. Gates and L. Delgado-Aparicio, Physical Review Letters **108**, 165004 (2012)
[35] D. K. Morozov, J. Phys.: Conf. Ser. **941**, 012009 (2017)
[36] T. Eich et al., Nucl. Fusion **58**, 034001 (2018)
[37] P. Zanca et al., Nucl. Fusion **59**, 126001 (2019)
[38] M. Giacomin et al., Phys. Rev. Lett. **128**, 185003 (2022)
[39] J. R. Harrison et al., Nucl. Fusion **59**, 112011 (2019)
[40] S. Kaye et al., Physics of Plasmas **8**, 1977 (2001)
[41] S. A. Sabbagh et al., Nucl. Fusion **41**, 1601 (2001)
[42] J W. Berkery et al., Plasma Physics and Controlled Fusion **65**, 045001 (2023)
[43] P. de Vries et al., Nucl Fusion **49**, 055011 (2009)
[44] S. P. Gerhardt et al., Nucl. Fusion **53**, 043020 (2013)
[45] J. Hugill, Nucl. Fusion **23**, 331 (1983)
[46] A. Stabler et al., Nucl. Fusion **32**, 1557 (1992)
[47] A. Pochelon et al., Proc. 22nd EPS Conf. on Controlled Fusion and Plasma Physics (Bournemouth, UK, 1995) vol 19C Part. IV, p 081
[48] A. Sykes et al., Nucl. Fusion **41**, 1423 (2001)

---

[49] A. Thornton, PhD. Thesis, University of York (2011)
[50] M. Huang et al., Plasma Physics and Controlled Fusion **58**, 125002 (2016)
[51] Y. S. Na et al., Proc. 41st EPS Conf. on Plasma Physics (Berlin, Germany, 2014) P4.028
[52] S. P. Gerhardt et al., Nucl. Fusion **53**, 063021 (2013)
[53] P. C. de Vries et al., Nucl. Fusion **58**, 026019 (2018)
[54] F. Poli et al., Proceedings of the IAEA Fusion Energy Conference 2018 pp EX/P7-27.
[55] J. E. Menard et al., Nucl. Fusion **52**, 083015 (2012)
[56] J. E. Menard et al., Nucl. Fusion **57**, 102006 (2017)
[57] V. Klevarova et al., Plasma Phys. Control. Fusion **62**, 025024 (2020)
[58] Q. Teng et al., Nucl. Fusion **56**, 106001 (2016)
[59] R. Budny et al., Nucl. Fusion **32**, 429 (1992)
[60] D. K. Morozov et al., Plasma Physics Reports **33**, 906 (2007)
[61] W. M. Stacey, Phys. Plasmas **4**, 1069 (1997)
[62] F. A. Kelly et al., Phys. Plasmas **8**, 4879 (2001)
[63] K. J. Montes et al., Nucl. Fusion **61**, 026022 (2021)
[64] M. Sertoli et al., Journal of Nucl. Mat. **463**, 837 (2015)
[65] M. L. Reinke et al., Nucl. Fusion **59**, 066003 (2019)
[66] A. J. Thornton et al., Plasma Phys. Control. Fusion **56**, 055008 (2014)
[67] B. Sieglin et al., Fusion Eng. And Design **191**, 113546 (2023)
[68] ITER Physics Expert Groups on Confinement and Transport and Confinement Modelling and Database and ITER Physics Basis Editors, Nucl. Fusion **39**, 2175 (1999)
[69] E. J. Doyle et al., Nucl. Fusion **47**, S18 (2007)
[70] J. E. Menard et al., Nucl. Fusion **52**, 083015 (2012)
[71] M. Maslov et al., Nucl. Fusion **60**, 036007 (2020)
[72] F. Ryter et al., Nucl. Fusion **61**, 046030 (2021)
[73] R. Scannell et al., Rev. Sci. Instrum. **81**, 10D520 (2010)
[74] H Reimerdes et al., Nucl. Fusion **62**, 042018 (2022)
[75] W. M. Stacey et al., Fusion Science and Technology **52**, 29 (2007)
[76] L. Delgado-Aparicio et al., Rev. Sci. Instrum. **85**, 11D859 (2014)